

Contents

S1.	Method optimization, validation, and application of LC-MS
S2.	Discussion on the uncertainty of semi-quantitative strategy
S3.	Strong BrC chromophores screening process based on partial least squares regression (PLS) model
S4.	Calculation method for the contribution of strong BrC chromophores to the total light absorption
S5.	Calculation method of glass transition temperature
S6.	Matrix effect evaluation
Table S1.	The relevant information of reference standards
Table S2.	The peak area, matrix effect of targeted analytes at the optimal concentration of four mobile additives and method detection limits (MDL), R^2 for standard curves, relative standard deviation (RSD) of the optimized method.
Table S3.	Identified HULIS structures in ambient aerosols
Table S4.	The deviations observed when different compounds were used as surrogate standards for quantifying each target analyte
Table S5.	Detailed chromatographic and mass spectrometric parameters used for the analysis of HULIS samples
Table S6.	Meteorological parameters and concentrations of pollutants in two haze events
Figure S1.	Schematic diagram of dataset and data normalization process.
Figure S2.	Components, R^2Y and Q^2 of the automatically fitted PLS model.
Figure S3.	Response permutation test results of PLS model.
Figure S4.	The VIP and coefficient list of each compound.
Figure S5.	Time series of meteorological factors and mass concentrations of gaseous pollutants and particulate matters during sampling period
Figure S6.	Schematic diagram of the MS/MS ion fragments for non-targeted HULIS species and their derivation processes
Figure S7.	The Pearson's correlation matrix between elemental composition, chemical structure and MAE_{365}
Figure S8.	Temporal variations in the mass fraction, light absorption contribution, and MAE_{365} values of 39 strong BrC chromophores
Figure S9.	The peak area comparison of 25 reference standards under different type of additives (A), mobile phase (B), additive concentration (C), and flow rate (D)
Figure S10.	The peak area comparison of 25 reference standards under different voltage (A), mass range (B), temperature of ion transfer tube (C) and vaporizer (D), and the proportion of sheath-auxiliary-sweep gas (E)
Figure S11.	3D waterfall diagram of total ions chromatogram for mixed standards at different flow rates of mobile phase

S1. Method optimization, validation, and application of LC-MS

25 representative standards (see **Table S1**) were selected to optimize the LC-MS method. These standards commonly found in HULIS samples from biomass burning (Hettiyadura et al., 2021; Huo et al., 2021; Li et al., 2020a; Wang et al., 2017a, b, 2019), coal combustion (Huang et al., 2023; Huo et al., 2021; Ma et al., 2023), secondary formation (Jaoui et al., 2023; Kojima et al., 2010; Lee and Lane, 2010; Li et al., 2021), and others (Yan et al., 2023; Zhou et al., 2022). Additionally, the elemental composition (i.e. CHO, CHN, CHON, CHOS, and CHONS) and structural differences (i.e. aromatic, aliphatic, and alicyclic structures) of HULIS were also taken into account for such selection.

Selection of mobile phase additives. We compared the detection efficiency of 25 standard compounds using four common mobile phase additives, i.e. formic acid (FA), acetic acid (AcOH), ammonium formate (AmFm), and ammonium acetate (AmAc) (Huang et al., 2020; Huo et al., 2021; Jemal et al., n.d.; Jin Yang et al., 2012; Liang et al., 2013; Song et al., 2022). **Figure S9A** showed the peak area of targeted analytes at the optimal concentration of four mobile additives, and indicated that AmFm were conducive to the signal enhancement of a few alkaloids (i.e. 1tBI and 3PAAE) and FA improved the most in the detection efficiency of some N-containing compounds (i.e. 1234THQ, 2N135T, and 4M5NC), while the more abundant CHO, CHN, CHON, CHOS, and CHONS species were detected at the highest efficiency by AcOH (detailed in **Table S2**). As a result, AcOH was selected as the best mobile phase additives in this study. The addition of AcOH increased the protonation yield of analytes but too high concentration of electrolytes will result in the loss of analyte signals (Kamel et al., 1999; Pan et al., 2006). In **Figure S9C**, it can be seen that an increase in the percentage of acetic acid caused an obvious increase of analyte signals, but acetic acid concentration higher than 0.05% v/v may cause a major decrease of analyte signals (e.g. ES, 910PheQ). It was worth mentioning that we also compared the difference between water / methanol and water / acetonitrile as mobile phases and the detection efficiency of all targeted analytes in water / acetonitrile was much lower than in water / methanol (**Figure S9B**). Therefore, we recommended that the mobile phase should be consistent with the sample solvent.

Elution rate of mobile phase. For C18 and other reversed-phase chromatographic columns, the separation performance is much sensitive to the elution rate (Lesellier et al., 2011; Louisi et al., 2006). **Figure S9D** indicated that the lower elution rate was beneficial to improving the sensitivity of analytes and thus facilitate the detection of trace HULIS species in atmosphere. However, the elution rate too low will cause the number of the theoretical plates and the column efficiency to plunge, resulting in the agglomeration of peaks (**Figure S11**). Therefore, we selected 0.2 mL min⁻¹ as the optimal elution rate.

Optimization of mass spectrometric parameters. We also compared the influence of mass spectrometric parameters on the detection efficiency of targeted analytes. Compared with chromatography, optimization of mass spectrometric parameters impacted less on the analyte signal when the analyte has been fully ionized. It will not be described in detail here and can be summarized (**Figure S10**) that (1) the higher the voltage was, the analyte signals increased but slightly. (2) An excessively wide mass range caused the signal intensity and stability of some compounds to decrease significantly, such as the signal of 4NP, 2N135T, and 3NSA with the condition of *m/z* 50-750 were much less than other conditions. (3) Elevating the ion transfer tube and vaporizer temperature within appropriate limits could significantly promote the ionization process of analytes. (4) The effect of different ratios of sheath gas and auxiliary gas on the ionization of analytes was neither regular nor significant.

Method validation and application. We calculated the method detection limits (MDLs,) of the optimized LC-MS method for 25 standard compounds based on 3 times of signal-to-noise ratio. The MDLs of these standards ranged from 0.001-0.48 ng mL⁻¹ (converted into 0.0008-0.38 ng m⁻³ in atmospheric concentration, **Table S2**). These MDLs were lower than MDLs from previous methods (Chow et al., 2015; Nyiri et al., 2016; Tao et al., 2024), which facilitated the discovery of non-targeted HULIS species with low concentrations.

All selected standards detected using this method showed good linear relationship between concentration and peak area (R^2 ranged from 0.9928-0.9997, **Table S2**). The matrix effects (described in **Section S2**) of most standards were below 15% (**Table S2**), indicating that ion enhancement or suppressions had little impact on the results. In addition, the precision (relative standard deviation, RSD) was less than 10% for all standards.

The application of this method in subsequent field samples successfully identified 264 species. CHO, CHON, and CHOS compounds were dominated species, which accounted for 47.9% - 66.8%, 18.0% - 42.1%, and 5.7% - 18.8% of all identified compounds, respectively. In terms of CHO and CHON categories, aromatic compounds were the main fraction (detailed in **Table S7**), including phenols, oxygenated polycyclic aromatic hydrocarbons, nitrophenols and other atmospheric organic species. These compounds were strongly related to fuel combustion. All of CHOS compounds were characterized by ion fragment m/z 96.9595 in the MS/MS spectra and were therefore identified as organosulfates (OSs). The majority of OSs, which can be summarized as the molecular formulas of C_nH_{2n+2}O₄₋₆S and C_nH_{2n}O₄₋₆S ($10 \leq n \leq 18$), were most probably derived from the secondary reaction of saturated or slightly unsaturated aliphatic hydrocarbons with SO₂.

Compared with previous studies (**Table S3**) (Chen et al., 2016; Claeys et al., 2012; Fan et al., 2018; Huang et al., 2020; Ma et al., 2020; Mukherjee et al., 2020; Stone et al., 2009; Voliotis et al., 2017; Zhang et al., 2022), we not only identified specific structure of HULIS species but also significantly improved the mass contribution of identified species. These included the newly identified 226 species, constituting 40.2% to 51.5% of the total HULIS mass. Among them were herbicides (e.g. diisopropylamine), Nicotine degradation products (e.g. 3-pyridylacetic acid), dyes (e.g. 2-methoxy-5-methylaniline and Michler's ketone), industrial chemicals (e.g. pyridine-2,6-dimethanol), personal care products (e.g. lauroylsarcosine), and explosive residue (e.g. 3,5-dinitrophenol), highlighting the method's capability in detecting unknown HULIS species. Overall, this optimized method can effectively detect the major species of atmospheric HULIS and provide invaluable insights into their composition and diversity.

S2. Discussion on the uncertainty of semi-quantitative strategy

In atmospheric chemistry, the components of organic aerosols are always complex and no authentic standards can be used for quantification. In the analysis of these components, it has been widely suggested to use available proxy compounds for quantification (Ma et al., 2022; Nozière et al., 2015). For example, camphor-10-sulfonic acid is often used as surrogate standard for the quantification of α -pinene derivative organosulfates (Ma et al., 2022; Nguyen et al., 2014). This strategy can achieve the quantitative analysis of various compounds in organic aerosols, but there are inevitable uncertainties which mainly come from the ionization efficiency difference between non-authentic standards and target analytes in mass spectrometric analysis (Nozière et al., 2015). Generally, the closer the molecular structure of surrogate standard is to the target analyte, the smaller the difference in ionization efficiency, resulting in the similar signal intensities in mass spectrometry.

Table S4 lists the deviation observed when different compounds were used as surrogate standards for quantification of each standard in this study. For instance, nitrophenol derivatives (4NP, 2N135T, and 4M5NC) showed quantification errors within 130% when used as surrogate standards for 26D4NP. Tetrahydroquinoline (1234THQ), an N-heterocyclic aromatic hydrocarbon, exhibited an error below 110% when quantifying 1tBI. However, even structurally similar surrogate standards may introduce an error of a factor over 2. Both P3C and I2C belong to N-heterocyclic aromatic aldehydes, yet using I2C as a surrogate for P3C resulted in a 46% error. When the structurally distinct PAAE was used as a surrogate for P3C, the error reached 600%. Therefore, when adopting semi-quantitative strategies, it is critical to first identify the chemical structure of the target analyte and subsequently select surrogate standards with analogous structural features for quantification.

S3. Strong BrC chromophores screening process based on partial least squares regression (PLS) model

The PLS model in Simca 14.1.0 software was used to screen strong BrC chromophores in this study. The principle of screening was based on the following assumption: the mass absorption efficiency of HULIS is equal to the weighted average of the mass absorption efficiency of its each component, which can be summarized as the formula (S1).

$$MAE_{365,HULIS} = \sum_i w_i MAE_{365,i} \quad (S1)$$

Where $MAE_{365,HULIS}$ represents the MAE_{365} of HULIS, $MAE_{365,i}$ represents the MAE_{365} of the number i compound in HULIS samples, w_i represents the mass contribution of the number i compound to the HULIS samples.

This model has been successfully applied to screen the key BrC molecules in organic aerosols by (Kuang et al., 2023). In this study, we screened the strong BrC chromophores of HULIS as the following principles: (1) variable importance for the projection (VIP) > 1; (2) regression coefficient (coeff) > 0; (3) belonging to aromatic CHON compounds; (4) detection ratio > 90%. The screening process of the PLS model was detailed as follows.

Firstly, we imported the data and set the mass fraction of each compound as the X-variable and the MAE_{365} of each sample as the Y-variable. Then the X-variables were scaled.

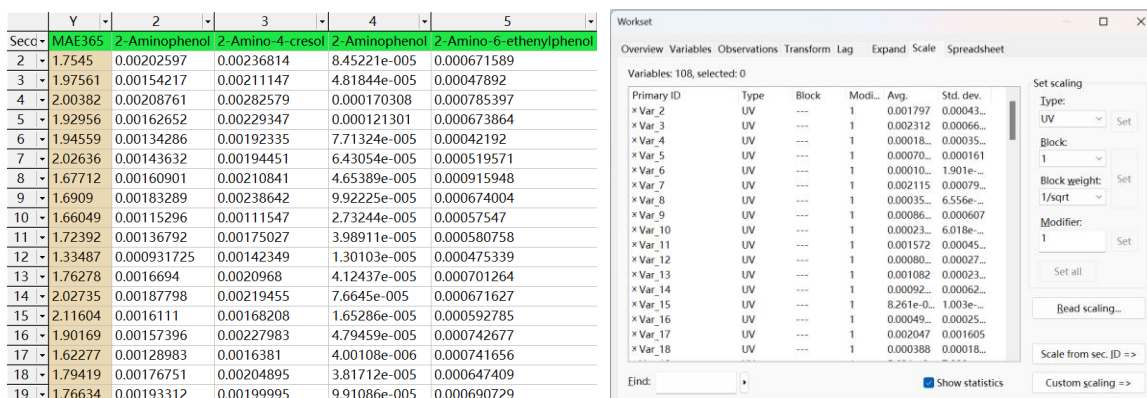


Figure S1. Schematic diagram of dataset and data normalization process. (Screenshot from SIMCA 14.1 software, Copyright © Sartorius Stedim Data Analytics AB)

Secondly, autofit the model using cross validation rules to determine the number of the significant components, and add component until R^2Y and Q^2 decrease. It is recommended that R^2Y and Q^2 are more than 0.5 and the difference between them is less than 0.3.

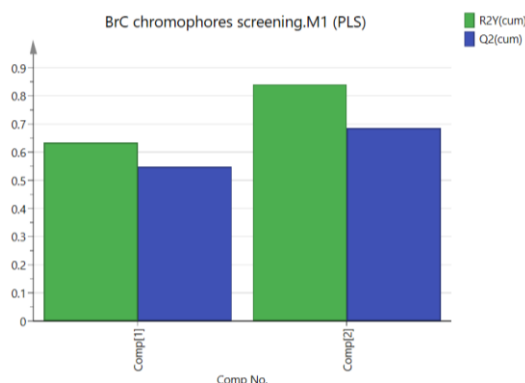


Figure S2. Components, R^2Y and Q^2 of the automatically fitted PLS model. (Screenshot from SIMCA 14.1 software, Copyright © Sartorius Stedim Data Analytics AB)

Thirdly, perform response permutation testing of the selected Y-variable. It is recommended that the intercept of R^2 and Q^2 should be less than 0.3 and 0.05 respectively.

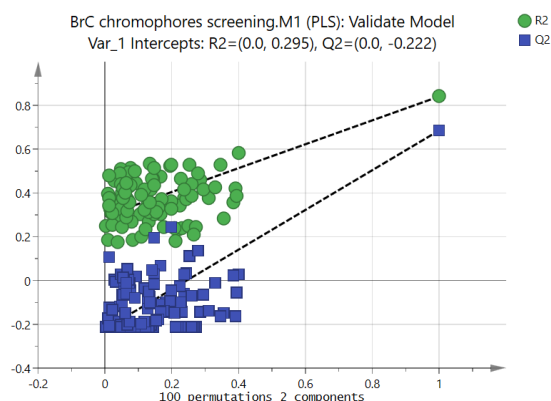


Figure S3. Response permutation test results of PLS model. (Screenshot from SIMCA 14.1 software, Copyright © Sartorius Stedim Data Analytics AB)

Finally, export the variable importance for the projection (VIP) and coefficient value of each compound calculated by the PLS model. The VIP value explains the importance of the independent X-variable to the dependent Y-variable. The coefficient greater than zero indicates that X-variable is positively correlated with Y-variable.

1	2	3	4	1	2	3	4
Var ID (Primary)	Var ID (Var. Sec. ID:1)	M1.VIP[2]	2.44693 * M1.VIP[2]cvSE	Var ID (Primary)	Var ID (Var. Sec. ID:1)	M1.CoeffCS[2](Var. 1)	2.44693 * M1.CoeffCS[2](Var. 1)cvSE
2 Var 69	4-Methyl-2-nitrobenzene-1,3-diol	1.74443	0.649467	2 Var 2	2-Aminophenol	0.00258402	0.0515663
3 Var 83	4,6-Dimethyl-2-nitrobenzene-1,3-diol	1.72873	0.884661	3 Var 3	2-Amino-4-cresol	-0.00136921	0.0448629
4 Var 96	4-Ethyl-3-(hydroxymethyl)-2-nitrophenol	1.66093	1.07548	4 Var 4	2-Aminophenol	0.00542233	0.0280378
5 Var 64	3,6-Dimethyl-2-nitrophenol	1.5491	0.661609	5 Var 5	2-Amino-6-ethenylphenol	-0.0147225	0.0647897
6 Var 76	1-(2-Methyl-5-nitrophenyl)ethanol	1.54396	0.50327	6 Var 6	3-Pyridylacetic acid	-0.0244832	0.0189326
7 Var 73	1-(4-Methyl-3-nitrophenyl)ethan-1-one	1.51693	0.435311	7 Var 7	2-Methoxy-5-methylaniline	-0.00625155	0.0411295
8 Var 82	2,3-Dimethyl-5-nitrobenzene-1,4-diol	1.49341	0.504874	8 Var 8	Pyridine-2,6-dimethanol	-0.0121636	0.0253226
9 Var 87	1-(2-Ethenyl-4-nitrophenyl)ethan-1-ol	1.47666	0.566255	9 Var 9	2-Amino-4-cresol	-0.0441551	0.0580503
10 Var 91	3,6-Diethyl-4-nitrophenol	1.47376	0.393309	10 Var 10	2-Formylindole	0.013755	0.0325866
11 Var 61	3-Nitrocatechol	1.45683	0.643635	11 Var 11	8-Hydroxyquinoline	-0.0115118	0.0429324
12 Var 102	2-Methyl-4-(4-nitrophenyl)but-3-en-1-ol	1.45337	0.82825	12 Var 12	1-Methyl-1H-indol-2-ol	-0.00275549	0.0229108
13 Var 67	3-Methyl-5-nitrocatechol	1.43318	0.380435	13 Var 13	Methyl-3-aminobenzoate	0.00570588	0.0461954
14 Var 68	4-Methyl-5-nitrocatechol	1.41632	0.415623	14 Var 14	3-Hydroxy-4-ethyl-1,2-benz	0.00266976	0.0382523
15 Var 80	2-(1-Hydroxyethyl)-4-nitrophenol	1.40602	0.238148	15 Var 15	1-Methoxy-2-(pyridin-3-yl)	-0.0349914	0.0255668
16 Var 9	2-Amino-4-cresol	1.38269	1.77447	16 Var 16	1H-Indene-3-carboxamide	0.0216069	0.0178253
17 Var 15	1-Methoxy-2-(pyridin-3-yl)ethan-1-ol	1.36681	0.871277	17 Var 17	1-(1H-Indol-3-yl)ethan-1-ol	-0.0103808	0.0259645
18 Var 93	2-(1-Hydroxyethyl)-3-methyl-4-nitrophenol	1.36656	0.305176	18 Var 18	2-Methyl-1,2-dihydrophthal	0.009931875	0.033515
19 Var 81	3,4-Dimethyl-5-nitrocatechol	1.31515	0.308317	19 Var 19	6-Amino-3,4-dihydro-1H-qu	0.00147662	0.0324627
20 Var 6	3-Pyridylacetic acid	1.28813	0.456705	20 Var 20	7-Hydroxy-1,2-dihydroquin	0.0095173	0.0377358
21 Var 95	3-(1-Hydroxyethyl)-2-methyl-4-nitrophenol	1.28539	0.457925	21 Var 21	Methyl 2-[hydrazinecarbon	0.00168096	0.0547629
22 Var 50	1-(2,4-Dihydroxyquinolin-3-yl)ethan-1-ol	1.28452	0.744024	22 Var 22	3-Pyridineacetic acid ethyl	-0.0126746	0.0250778
23 Var 65	2,6-Dimethyl-4-nitrophenol	1.27123	0.963451	23 Var 23	6-Ethenyl-5-ethyl-1,2,3,4-te	0.00656912	0.0364175
24 Var 103	2-Ethyl-4,6-dimethyl-5-nitrobenzene-1,3	1.26507	0.474343	24 Var 24	2-sec-Butyl-3-methoxysura	-0.00310125	0.0382659

Figure S4. The VIP and coefficient list of each compound. (Screenshot from SIMCA 14.1 software, Copyright © Sartorius Stedim Data Analytics AB)

S4. Calculation method for the contribution of strong BrC chromophores to the total light absorption

To quantify the light absorbance contribution of the identified strong BrC chromophores at a wavelength of 365 nm, we established the following calculation scheme.

$$MAE_{strong,365} = \frac{MAE_{obs,365} \times C - MAE_{others,365} \times (C - C_{strong})}{C_{strong}} \quad (S2)$$

$$Light\ absorption\ contribution_{strong,365} = \frac{MAE_{strong,365} \times C_{strong}}{MAE_{obs,365} \times C} \quad (S3)$$

Where $MAE_{strong,365}$ represents the MAE_{365} of strong BrC chromophores, $MAE_{obs,365}$ is the observed MAE_{365} of the HULIS samples, C_{strong} represents the carbon mass concentration of the strong BrC chromophores. $MAE_{others,365}$ is the MAE_{365} of components other than the strong BrC chromophores in HULIS, expressed as the intercept (set as $1.3615 \text{ m}^2 \text{ gC}^{-1}$, see **Figure 3** in **Section 3.3**) of the linear equation between the mass fraction of strong BrC chromophores with the $MAE_{obs,365}$.

S5. Calculation method of glass transition temperature.

The glass transition temperature (T_g) of HULIS was an important parameter for evaluating its phase state. According to a series of developed parameterizations (Li et al., 2020b), this study calculated the T_g of HULIS as follows:

$$T_{g,CHO} = (n_c^0 + \ln(n_c))b_c + \ln(n_H)b_H + \ln(n_C)\ln(n_H)b_{CH} + \ln(n_O)b_O + \ln(n_C)\ln(n_O)b_{CO} \quad (S4)$$

$$T_{g,org} = \sum_i w_i T_{g,i} \quad (S5)$$

$$T_g = \frac{(1-w_{org})T_{g,w} + \frac{1}{k_{GT}}w_{org}T_{g,org}}{(1-w_{org}) + \frac{1}{k_{GT}}w_{org}} \quad (S6)$$

The glass transition temperature of a certain compound under dry condition could be calculated based on its molecular formula. For example, Equation (S4) illustrated the calculation method of the glass transition

temperature of CHO compounds, the value of n_C , n_H , and n_O represented the number of carbon, hydrogen, and oxygen atom, the coefficients n_C^0 , b_C , b_H , b_{CH} , b_O , and b_{CO} were 12.13, 10.95, -41.81, 21.61, 118.96, and -24.38. For CHON and CHOS compounds, they could be also calculated by parameterizations developed by (Li et al., 2020b). The bulk glass transition temperature of organic matters was equal to the weighted average of the glass transition temperature of each compound ($T_{g,i}$, as equation (S5)). In equation (S6), T_g represented the glass transition temperature of organic-water mixtures, k_{GT} was the Gordon-Taylor constant (suggested to be 2.5) for organic-water mixtures, w_{org} was the mass fraction of organic matters in the model of organic-water mixtures and the water content could be estimated using the effective hygroscopicity parameter (Petters and Kreidenweis, 2007).

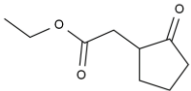
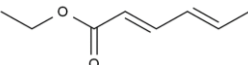
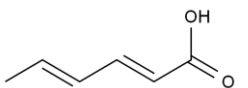
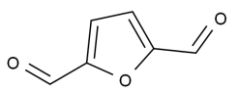
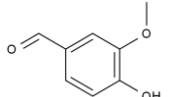
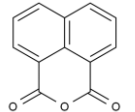
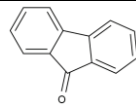
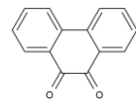
S6. Matrix effect evaluation.

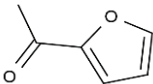
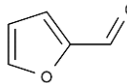
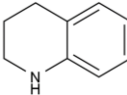
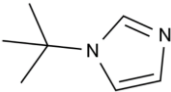
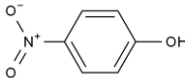
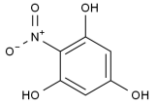
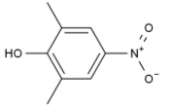
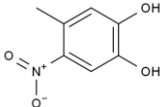
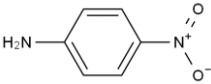
It has been widely accepted that matrix constituents can influence analyte ionization, calibration curves, and signal responses, which was referred to the matrix effect (ME) (Antignac et al., 2005; Nasiri et al., 2021; Pizzutti et al., 2016). The ME (%) can be calculated via the following equation:

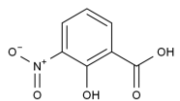
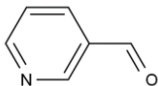
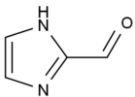
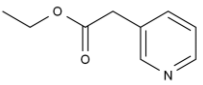
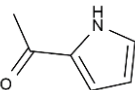
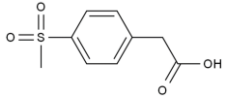
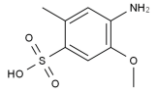
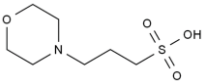
$$ME (\%) = \left(\frac{\text{peak area std in blank matrix}}{\text{peak area std in solvent}} - 1 \right) \times 100 \quad (S7)$$

In this equation, ME (%) refers to the percentage of matrix effect calculated by the peak area data from the analytical solutions in blank matrix extract and in organic solvent (methanol). If ion suppression occurs, it will cause negative values while ion enhancement will result in positive values.

Table S1. The relevant information of reference standards

Compound	Abbreviation	Structure	Formula	<i>m/z</i> & preferred ion	Category	Subcategory	Reference Sample
Ethyl-2-oxocyclopentylacetate	E2OCA		C ₉ H ₁₄ O ₃	171.1016 [M+H] ⁺	CHO	Alicyclics	
Ethyl sorbate	ES		C ₈ H ₁₂ O ₂	141.0910 [M+H] ⁺		Aliphatics	
Sorbic acid	SA		C ₆ H ₈ O ₂	113.0597 [M+H] ⁺			Biomass burning(Hettiyadura et al., 2021; Huo et al., 2021)
Furan-2,5-dicarbaldehyde	F25DC		C ₆ H ₄ O ₃	125.0233 [M+H] ⁺			
Vanillin	VAN		C ₈ H ₈ O ₃	153.0546 [M+H] ⁺			Coal combustion (Huo et al., 2021), Snowpack (Zhou et al., 2022) & Biomass burning (Huo et al., 2021; Lin et al., 2012)
1,8-Naphthalic anhydride	18NaPA		C ₁₂ H ₆ O ₃	199.0390 [M+H] ⁺		Aromatics	Secondary formation (Kojima et al., 2010), Coal combustion (Huo et al., 2021) & Biomass burning (Huo et al., 2021)
9-Fluorenone	9FLU		C ₁₃ H ₈ O	181.0648 [M+H] ⁺			Coal combustion (Huo et al., 2021)
9,10-Phenanthrenequinone	910PheQ		C ₁₄ H ₈ O ₂	209.0597 [M+H] ⁺			Secondary formation (Lee and Lane, 2010)

2-Acetylfuran	2AF		C ₆ H ₆ O ₂	111.0441 [M+H] ⁺			
2-Furaldehyde	2FA		C ₅ H ₄ O ₂	97.0284 [M+H] ⁺			
1,2,3,4-Tetrahydroquinoline	1234THQ		C ₉ H ₁₁ N	134.0964 [M+H] ⁺	CHN	Aromatics	Biomass burning (Wang et al., 2019)
1-t-Butylimidazole	1tBI		C ₇ H ₁₂ N ₂	125.1073 [M+H] ⁺			Biomass burning (Wang et al., 2017b)
4-Nitrophenol	4NP		C ₆ H ₅ NO ₃	140.0342 [M+H] ⁺	CHON	Aromatics	
2-Nitrobenzene-1,3,5-triol	2N135T		C ₆ H ₅ NO ₅	170.0084 [M-H] ⁻			Secondary formation (Jaoui et al., 2023)
2,6-Dimethyl-4-nitrophenol	26D4NP		C ₈ H ₉ NO ₃	166.0499 [M-H] ⁻			Coal combustion (Huo et al., 2021) & Biomass burning (Huo et al., 2021)
4-Methyl-5-nitrocatechol	4M5NC		C ₇ H ₇ NO ₄	168.0291 [M-H] ⁻			Secondary formation (Li et al., 2020a, 2021), Biomass burning (Li et al., 2020a) & Diesel (Yan et al., 2023)
4-Nitroaniline	4NA		C ₆ H ₆ N ₂ O ₂	139.0502 [M+H] ⁺			Ambient aerosol (Kuang et al., 2023)

3-Nitrosalicylic acid	3NSA		C ₇ H ₅ NO ₅	182.0084 [M-H] ⁻		Biomass burning (Wang et al., 2017a)		
Pyridine-3-carbaldehyde	P3C		C ₆ H ₅ NO	108.0444 [M+H] ⁺				
Imidazole-2-carboxaldehyde	I2C		C ₄ H ₄ N ₂ O	97.0396 [M+H] ⁺		Secondary formation (Kampf et al., 2012)		
3-Pyridineacetic acid ethyl	3PAAE		C ₉ H ₁₁ NO ₂	166.0863 [M+H] ⁺				
2-Acetyl pyrrole	2AP		C ₆ H ₇ NO	110.0600 [M+H] ⁺				
4-(Methylsulfonyl) phenylacetic acid	4MSPAA		C ₉ H ₁₀ O ₄ S	215.0373 [M+H] ⁺	CHOS	Aromatics	Snowpack (Zhou et al., 2022)	
4-Amino-5-methoxy-2-methylbenzenesulfonic acid	4A5M2MBSA		C ₈ H ₁₁ NO ₄ S	218.0482 [M+H] ⁺	CHONS	Aromatics		
3-Morpholin-4-ylpropane-1-sulfonic acid	3M4P1SA		C ₇ H ₁₅ NO ₄ S	210.0795 [M+H] ⁺		Alicyclics		

193 **Table S2.** The peak area, matrix effect of targeted analytes at the optimal concentration of four mobile additives and method detection limits (MDL), R² for standard
 194 curves, relative standard deviation (RSD) of the optimized method.

Compounds	Control		1mM AmFm		1Mm AmAc		0.05% v/v FA		0.05% v/v AcOH		MDL ng m ⁻³	R ² for standard curves	RSD %
	Peak Area	ME%	Peak Area	ME%	Peak Area	ME%	Peak Area	ME%	Peak Area	ME%			
E2OCA	2.8E+7	2.5	4.2E+7	5.8	3.2E+7	24.8	3.7E+7	1.3	5.7E+7	8.5	0.0098	0.9997	0.6
ES	1.9E+4	-1	3.2E+5	-11.1	2.3E+5	-10.3	3.8E+5	3.2	8.1E+5	-4.1	0.38	0.9940	1.5
SA	1.4E+4	6.7	1.7E+5	-19.5	1.3E+5	-20.2	3.2E+5	5.1	2.4E+5	11.6	0.10	0.9926	3.4
F25DC	2.4E+5	1.6	8.0E+5	25.7	7.3E+5	22.4	1.1E+6	0.0	1.4E+6	3.7	0.10	0.9926	4.8
VAN	1.1E+6	6.1	1.4E+6	8.3	7.4E+5	30.2	3.0E+6	6.2	4.1E+6	6.3	0.011	0.9992	2.2
18NaPA	1.1E+6	7	3.9E+6	8.2	4.5E+6	3.1	4.8E+6	4.8	6.9E+6	11.2	0.012	0.9972	1.9
9FLU	1.8E+6	8.9	2.8E+6	8.3	4.3E+6	25.1	2.7E+6	0.0	6.2E+6	5.9	0.12	0.9989	1.3
910PheQ	3.6E+7	6.6	4.4E+7	7.1	6.2E+7	23.5	3.8E+7	1.6	8.9E+7	8.8	0.0022	0.9991	5.4
2AF	2.3E+4	8.3	6.0E+5	4.5	5.1E+5	7.9	6.7E+5	4.6	6.4E+5	1.2	0.012	0.9954	3.7
2FA	2.7E+4	5.5	1.3E+5	24.5	1.1E+5	27.8	7.4E+4	19.1	1.2E+5	12.2	0.26	0.9925	5.0
1234THQ	1.2E+5	2.5	8.7E+5	-5.8	7.0E+5	-27.8	1.4E+7	0.4	1.1E+7	0.3	0.0052	0.9943	4.7
1tBI	1.5E+7	3.4	1.8E+7	21.2	1.2E+7	4.2	1.0E+7	1.8	1.0E+7	13.1	0.0048	0.9993	5.8
4NP	6.4E+4	-11.9	8.5E+4	-2.2	1.0E+5	36.4	1.2E+5	1.3	1.7E+5	-1.0	0.035	0.9934	8.6
2N135T	3.1E+6	6.6	2.0E+6	22.6	1.1E+6	19.1	6.7E+6	10.6	3.4E+6	3.1	0.039	0.9971	6.1
26D4NP	4.7E+6	1.3	1.6E+6	-1.7	3.5E+6	51.1	3.0E+6	2.8	3.4E+6	16.6	0.0075	0.9932	7.3
4M5NC	1.9E+6	12.9	3.1E+5	33.6	1.0E+5	160.9	6.2E+6	11.9	4.0E+6	0.3	0.018	0.9956	4.2
4NA	2.9E+6	0.2	4.9E+6	5.6	4.5E+6	6.0	6.0E+6	5.7	7.9E+6	-0.1	0.017	0.9989	2.1
3NSA	3.5E+5	8.2	3.1E+5	39.9	1.2E+6	39.3	6.2E+5	19.3	1.9E+5	11.9	0.37	0.9939	7.8
P3C	1.5E+6	6.7	6.1E+6	16.6	5.4E+6	19.8	8.8E+6	-0.4	1.0E+7	5.3	0.0094	0.9991	9.4
I2C	3.2E+6	2.6	7.1E+6	5.5	3.7E+6	16.8	5.3E+6	-1.7	6.8E+6	-0.5	0.016	0.9995	4.6
3PAAE	2.3E+8	7.9	4.2E+8	9.3	2.2E+8	20.4	2.5E+8	14.4	2.9E+8	13.4	0.00079	0.9979	8.7
2AP	4.9E+5	4.6	7.7E+5	4.3	6.9E+5	20.2	1.8E+6	5.9	2.6E+6	0.3	0.016	0.9964	7.8
4MSPAA	1.4E+5	2	1.9E+6	-88.9	1.7E+5	22.7	2.9E+6	21.3	3.9E+6	14.3	0.010	0.9955	9.4
4A5M2MBSA	8.1E+5	5.5	9.8E+5	3.0	1.4E+6	12.9	7.4E+5	3.9	1.3E+6	4.0	0.040	0.9928	8.9
3M4P1SA	6.4E+6	1.3	9.0E+6	0.3	8.7E+6	15.7	2.5E+6	1.7	5.2E+6	5.6	0.031	0.9980	3.4

196 **Table S3.** Identified HULIS structures in ambient aerosols

Reference	Identification Level	Numbers	Instrument	Quantification	Identification Method	Contribution to HULIS Mass
(Claeys et al., 2012)	Specific Structure	3	LC-PDA-MS	Yes	Standards Matching	0.34 - 1.2%
(Huang et al., 2020)	Specific Structure	18	LC-PDA-MS	Yes	Standards Matching	1 - 14% (light absorption contribution)
(Ma et al., 2020)	Specific Structure	16	GC-MS	Yes	Standards Matching	1.4 – 5.4%
(Fan et al., 2018)	Specific Structure	27	TMAH-GC-MS	None	Ion Fragments Matching	Unknown
(Chen et al., 2016)	Functional Group	N.A.	FTIR	Yes	Peak Wavelength Matching	100.8 - 101.1%
(Zhang et al., 2022)	Functional Group	N.A.	FTIR	None	Peak Wavelength Matching	Unknown
(Mukherjee et al., 2020)	Functional Group	N.A.	FTIR	None	Peak Wavelength Matching	Unknown
(Voliotis et al., 2017)	Functional Group	N.A.	FTIR	None	Peak Wavelength Matching	Unknown
(Stone et al., 2009)	Functional Group	N.A.	LC-MS/MS	None	Ion Fragments Matching	Unknown
This study	Specific Structure	264	UHPLC-HRMS/MS	Yes	Standards Matching & Ion Fragments Matching	38.2 – 78.1%

Table S4. The deviations observed when different compounds were used as surrogate standards for quantifying each target analyte

Deviation %	E2OCA	ES	SA	F25DC	VAN	18NaPA	9FLU	910PheQ	2AF	2FA	1234THQ	1tBI	4NP
E2OCA	100.0	4.3	8.8	17.6	101.9	64.2	9.5	324.7	21.7	2.5	163.1	155.8	93.5
ES	2400.0	100.0	207.6	421.0	2446.7	1539.0	224.3	7799.2	519.1	57.3	3916.1	3741.7	3014.4
SA	1164.8	47.8	100.0	203.7	1187.5	746.6	108.1	3787.0	251.3	27.0	1901.1	1816.4	1018.8
F25DC	570.7	23.7	49.2	100.0	581.8	365.9	53.2	1854.7	123.3	13.5	931.2	889.7	625.2
VAN	98.1	4.8	9.1	17.8	100.0	63.2	9.8	317.2	21.8	3.0	159.6	152.6	125.5
18NaPA	155.5	7.3	14.2	27.9	158.5	100.0	15.3	503.5	34.3	4.5	253.2	242.0	51.2
9FLU	1079.1	44.1	92.5	188.5	1100.1	691.6	100.0	3508.8	232.7	24.9	1761.4	1682.8	785.6
910PheQ	30.3	0.6	2.0	4.7	30.9	19.2	2.2	100.0	6.0	0.1	49.9	47.6	28.5
2AF	463.1	19.1	39.9	81.1	472.1	296.9	43.1	1505.4	100.0	10.9	755.8	722.1	409.9
2FA	4219.8	175.1	364.2	739.6	4301.9	2705.6	393.7	13714.5	912.1	100.0	6885.9	6579.1	4191.6
1234THQ	61.2	2.2	5.0	10.5	62.4	39.1	5.4	199.5	13.0	1.1	100.0	95.5	60.7
1tBI	64.0	2.3	5.2	10.9	65.3	40.9	5.6	208.9	13.5	1.2	104.7	100.0	60.9
4NP	106.9	3.3	9.8	16.0	79.7	195.5	12.7	351.1	24.4	2.4	164.7	164.2	100.0
2N135T	103.7	3.2	9.5	15.5	77.3	186.1	12.3	339.9	23.7	2.3	159.6	159.1	97.0
26D4NP	91.1	3.8	7.9	16.0	92.9	58.4	8.5	296.1	19.7	2.2	148.7	142.1	86.3
4M5NC	110.6	4.4	9.4	19.3	112.7	70.9	10.2	359.8	23.8	2.5	180.6	172.5	123.6
4NA	131.5	5.5	11.4	23.1	134.1	84.3	12.3	427.5	28.4	3.1	214.6	205.1	184.7
3NSA	2423.3	100.5	209.1	424.7	2470.4	1553.7	226.0	7875.9	523.8	57.4	3954.4	3778.2	5453.3
P3C	91.3	4.0	8.1	16.2	93.0	58.6	8.7	296.1	19.9	2.4	148.8	142.2	92.6
I2C	200.5	8.3	17.3	35.1	204.4	128.5	18.7	651.6	43.3	4.7	327.1	312.6	209.9
3PAAE	15.4	0.8	1.4	2.8	15.7	9.9	1.5	49.6	3.4	0.5	25.0	23.9	14.1
2AP	132.3	5.5	11.4	23.2	134.9	84.8	12.3	430.1	28.6	3.1	215.9	206.3	210.9
4MSPAA	139.6	6.0	12.3	24.7	142.3	89.6	13.3	453.2	30.4	3.6	227.7	217.6	163.9
4A5M2MBSA	1347.0	55.3	115.7	235.6	1373.2	863.5	125.1	4379.3	290.7	31.3	2198.5	2100.5	1400.4
3M4P1SA	763.1	31.3	65.5	133.4	778.0	489.1	70.8	2481.0	164.6	17.7	1245.5	1190.0	1021.5

Deviation %	2N135T	26D4NP	4M5NC	4NA	3NSA	P3C	I2C	3PAAE	2AP	4MSPAA	4A5M2MBSA	3M4P1SA
E2OCA	96.4	109.7	90.4	76.1	4.3	109.6	50.0	654.7	75.6	71.6	7.6	13.3
ES	3108.7	2634.1	2170.5	1824.8	99.5	2630.1	1197.5	15728.3	1814.0	1717.7	179.6	315.9
SA	1050.7	1278.5	1053.3	885.5	47.5	1276.6	580.8	7637.8	880.2	833.4	86.4	152.6
F25DC	644.8	626.3	516.1	433.9	23.5	625.4	284.7	3740.5	431.3	408.4	42.6	75.0
VAN	129.4	107.6	88.8	74.8	4.7	107.4	49.3	639.0	74.3	70.4	8.0	13.5
18NaPA	53.7	170.6	140.7	118.4	7.2	170.3	78.0	1014.6	117.7	111.5	12.4	21.2
9FLU	810.2	1184.4	975.8	820.3	43.8	1182.7	537.9	7076.9	815.4	772.0	79.9	141.2
910PheQ	29.4	33.3	27.3	22.9	0.6	33.3	14.8	202.4	22.7	21.5	1.6	3.4
2AF	422.7	508.3	418.8	352.1	19.0	507.5	230.9	3036.0	350.0	331.4	34.5	60.8
2FA	4322.7	4631.4	3816.1	3208.3	174.2	4624.5	2105.0	27658.2	3189.2	3019.8	315.1	554.8
1234THQ	62.6	67.2	55.3	46.4	2.2	67.1	30.3	402.6	46.1	43.7	4.3	7.8
1tBI	62.8	70.3	57.8	48.6	2.3	70.2	31.7	421.6	48.3	45.7	4.4	8.1
4NP	103.1	115.8	80.9	54.2	1.8	108.0	47.6	708.2	47.4	61.0	7.1	9.8
2N135T	100.0	112.3	78.4	52.5	1.8	104.7	46.2	687.0	46.0	59.2	6.9	9.5
26D4NP	89.0	100.0	82.4	69.3	3.8	99.8	45.4	597.2	68.9	65.2	6.8	12.0
4M5NC	127.5	121.4	100.0	84.0	4.4	121.2	55.1	725.7	83.5	79.1	8.1	14.4
4NA	190.4	144.4	118.9	100.0	5.4	144.1	65.6	862.1	99.4	94.1	9.8	17.3
3NSA	5623.9	2659.7	2191.5	1842.4	100.0	2655.7	1208.8	15883.5	1831.5	1734.2	180.9	318.6
P3C	95.5	100.2	82.6	69.4	4.0	100.0	45.6	597.0	69.0	65.4	7.0	12.2
I2C	216.5	220.0	181.3	152.4	8.3	219.7	100.0	1314.0	151.5	143.5	15.0	26.4
3PAAE	14.6	16.9	13.9	11.7	0.8	16.8	7.7	100.0	11.6	11.0	1.3	2.1
2AP	217.5	145.2	119.7	100.6	5.4	145.0	66.0	867.4	100.0	94.7	9.9	17.4
4MSPAA	169.0	153.2	126.3	106.2	6.0	153.0	69.8	913.8	105.6	100.0	10.7	18.6
4A5M2MBSA	1444.2	1478.5	1218.1	1024.0	55.0	1476.3	671.6	8832.5	1017.9	963.8	100.0	176.6
3M4P1SA	1053.5	837.6	690.1	580.1	31.1	836.3	380.5	5003.8	576.6	546.0	56.6	100.0

Table S5. Detailed chromatographic and mass spectrometric parameters used for the analysis of HULIS samples.

Instrument	Ultimate 3000 Liquid Chromatography-Orbitrap Fusion™ Tribrid™ Mass Spectrometer
LC settings	Column
	Accucore C18 100 × 2.1 mm 2.6 μm, Thermo Fisher Scientific
	Injection Volume
	3 μL
	Mobile Phases
	Phase A: ultrapure water +0.05% acetic acid Phase B: methanol +0.05% acetic acid
	Solvent Flow
	0.2 mL/min
	Column temperature
	35°C
MS settings	Gradient
	Time(min)
	%A
	%B
	0
	80
	2
	80
	17
	0
MS/MS settings	19
	0
	100
	20
	80
	20
	23
	80
	20
	Ion Source Type
MS settings	H-ESI
	Spray Voltage
	Positive: 3500 V; Negative: 3250 V
	Gas Flow (arb)
	Sheath: 35; Auxiliary: 10, Sweep: 0
	Temperature
	Ion transfer tube: 320°C, Vaporizer: 125°C
	Mass range
	60-600
	Orbitrap Resolution
MS/MS settings	120 000
	RF lens (%)
	60
	Filter criteria
	Dynamic exclusion: exclude ions after 3 times if they occur within 25 s and exclusion duration set as 100 s
	Data dependent mode
	Cycle time
	Time between Master Scans
	1 s
	Activation type
MS/MS settings	HCD
	Collision Energy (%)
	40 ± 10
	Detector type
	Orbitrap
	Resolution
	15 000

207 **Table S6.** Meteorological parameters and concentrations of pollutants during two haze events,
208 clean day, and overall period.

Parameters	Event I	Event II	Clean day	Overall
PM _{2.5} ($\mu\text{g}/\text{m}^3$)	159.5 \pm 53.8	83.7 \pm 36.4	14.1 \pm 11.9	50.7 \pm 34.3
HULIS-C ($\mu\text{gC}/\text{m}^3$)	6.68	4.65	0.97	2.97 \pm 1.54
OC ($\mu\text{gC}/\text{m}^3$)	27.8	16.6	4.6	11.7 \pm 5.7
EC ($\mu\text{gC}/\text{m}^3$)	3.2	4.6	1.3	2.1 \pm 0.9
OC/EC	8.7	3.6	3.6	5.7 \pm 1.4
Na ⁺ ($\mu\text{g}/\text{m}^3$)	0.33	0.37	0.07	0.21 \pm 0.13
K ⁺ ($\mu\text{g}/\text{m}^3$)	1.89	7.20	0.25	1.66 \pm 2.43
NH ₄ ⁺ ($\mu\text{g}/\text{m}^3$)	20.65	4.30	1.32	4.32 \pm 4.09
Cl ⁻ ($\mu\text{g}/\text{m}^3$)	5.69	7.29	0.77	3.06 \pm 1.92
NO ₃ ⁻ ($\mu\text{g}/\text{m}^3$)	41.56	6.79	2.09	7.40 \pm 8.80
SO ₄ ²⁻ ($\mu\text{g}/\text{m}^3$)	16.66	7.30	1.32	4.09 \pm 3.51
SO ₂ ($\mu\text{g}/\text{m}^3$)	20.9 \pm 5.3	25.1 \pm 15.1	10.6 \pm 4.2	18.1 \pm 8.8
NO ₂ ($\mu\text{g}/\text{m}^3$)	69.5 \pm 12.6	31.5 \pm 13.3	11.3 \pm 5.2	33.6 \pm 19.4
O ₃ ($\mu\text{g}/\text{m}^3$)	14.2 \pm 10.4	33.1 \pm 19.2	64.9 \pm 7.2	35.7 \pm 18.6
CO (mg/m ³)	1.56 \pm 0.34	0.79 \pm 0.20	0.27 \pm 0.10	0.65 \pm 0.36
Relative Humidity (%)	83.1 \pm 4.6	61.9 \pm 14.0	51.6 \pm 8.7	60.9 \pm 13.8
Temperature (°C)	-10.0 \pm 4.1	-18.3 \pm 4.3	-10.9 \pm 4.4	-13.3 \pm 6.8
Wind Speed (m/s)	1.6 \pm 0.6	1.7 \pm 0.9	1.7 \pm 0.5	3.3 \pm 1.8

209

210

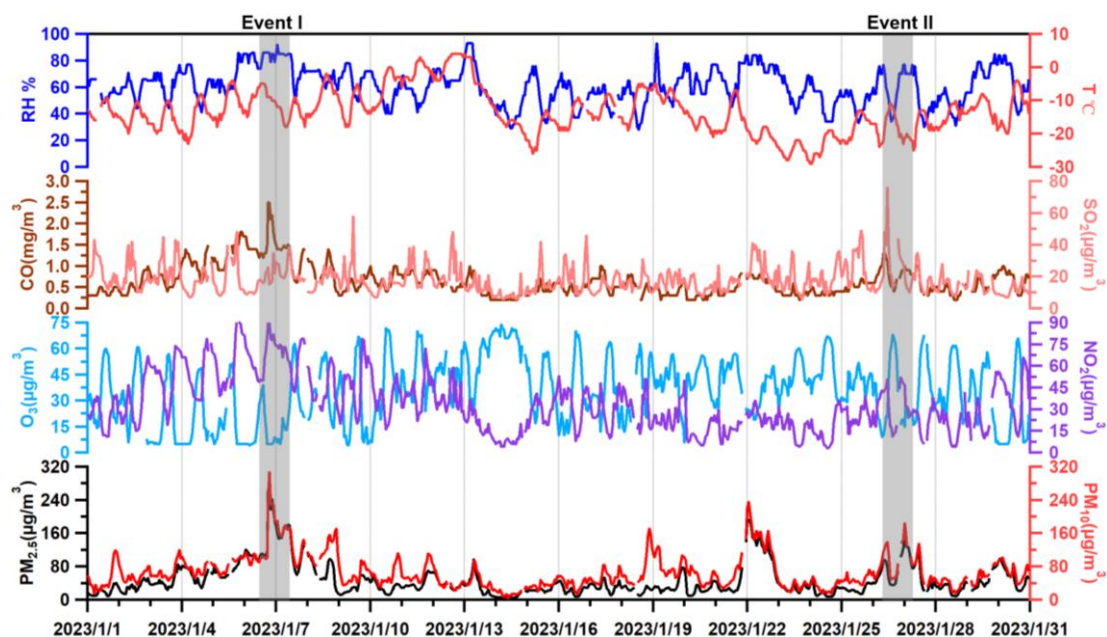


Figure S5. Time series of meteorological factors and mass concentrations of gaseous pollutants and particulate matters during sampling period.

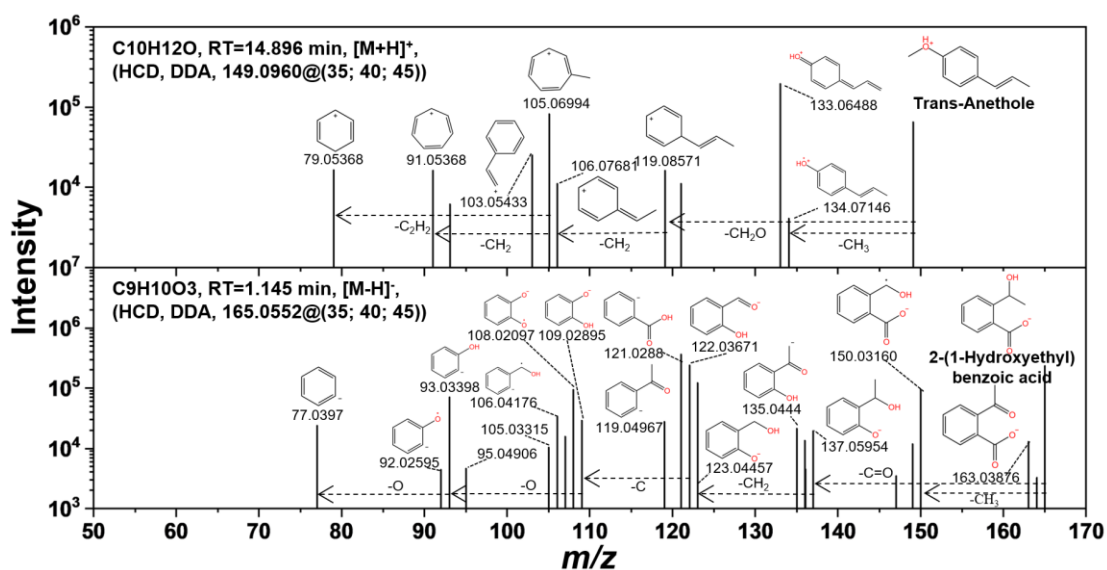


Figure S6. Schematic diagram of the MS/MS ion fragments for non-targeted HULIS species and their derivation processes.

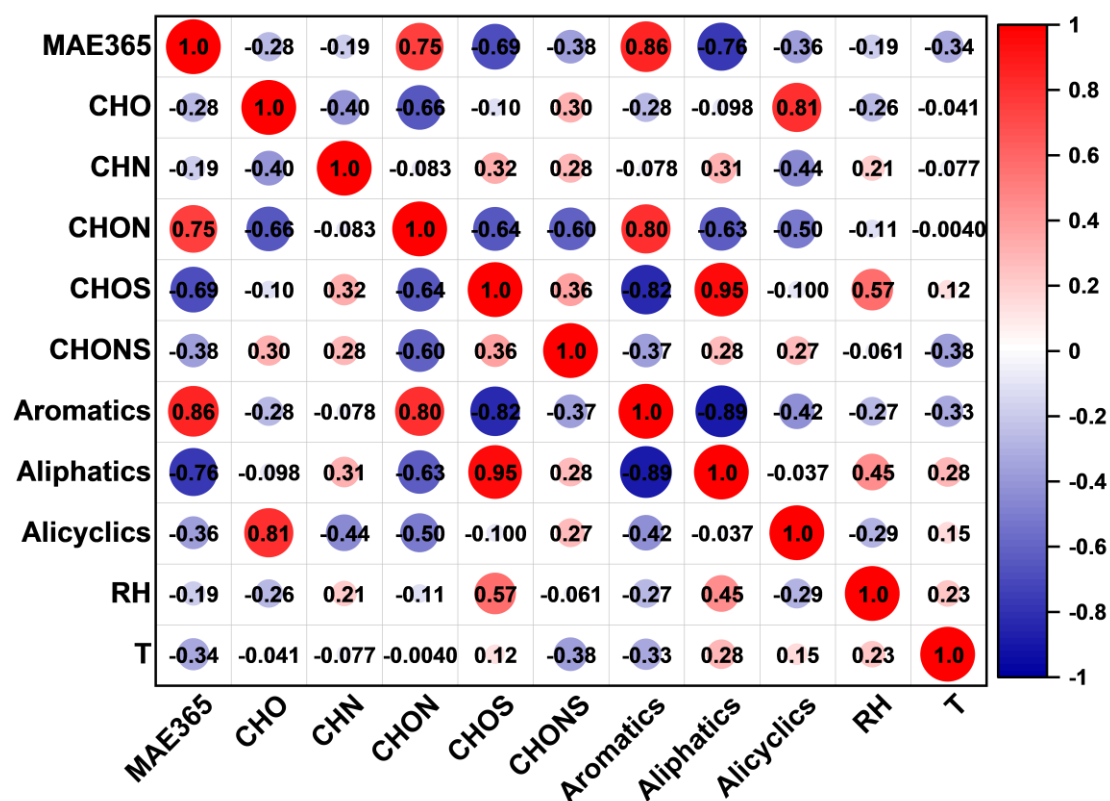


Figure S7. The Pearson's correlation matrix between elemental composition, chemical structure, MAE₃₆₅, relative humidity, and ambient temperature.

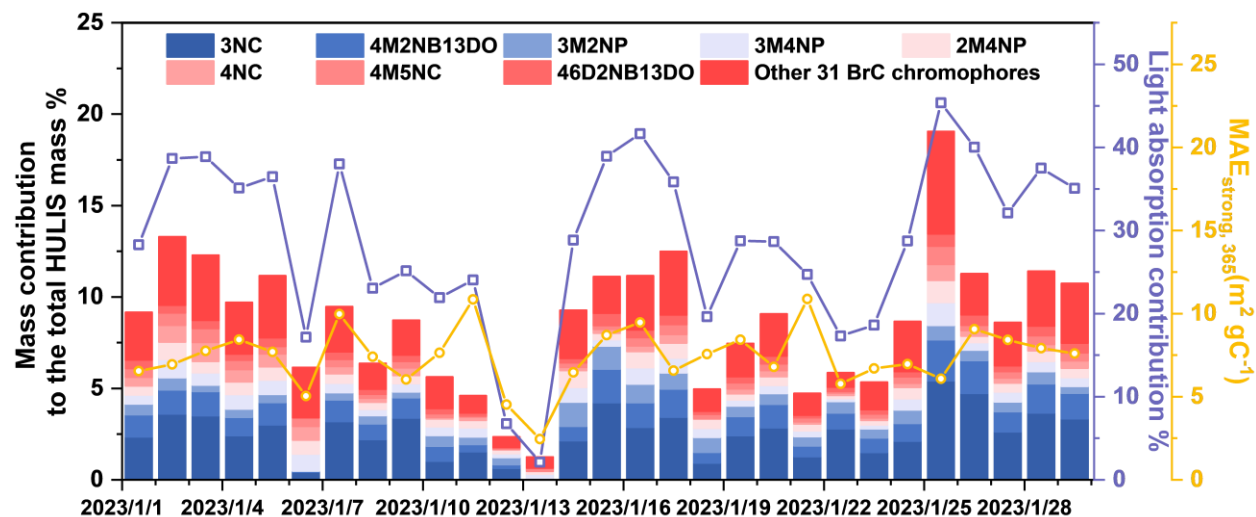


Figure S8. Temporal variations in the mass fraction, light absorption contribution, and MAE₃₆₅ values of 39 strong BrC chromophores. The abbreviations of 3NC, 4M2NB13DO, 3M2NP, 3M4NP, 2M4NP, 4NC, 4M5NC, 26D4NP, and 46D2NB13DO represented 3-nitrocatechol, 4-methyl-2-nitrobenzene-1,3-diol, 3-methyl-2-nitrophenol, 3-methyl-4-nitrophenol, 2-methyl-4-nitrophenol, 4-nitrocatechol, 4-methyl-5-nitrocatechol, and 4,6-dimethyl-2-nitrobenzene-1,3-diol, respectively.

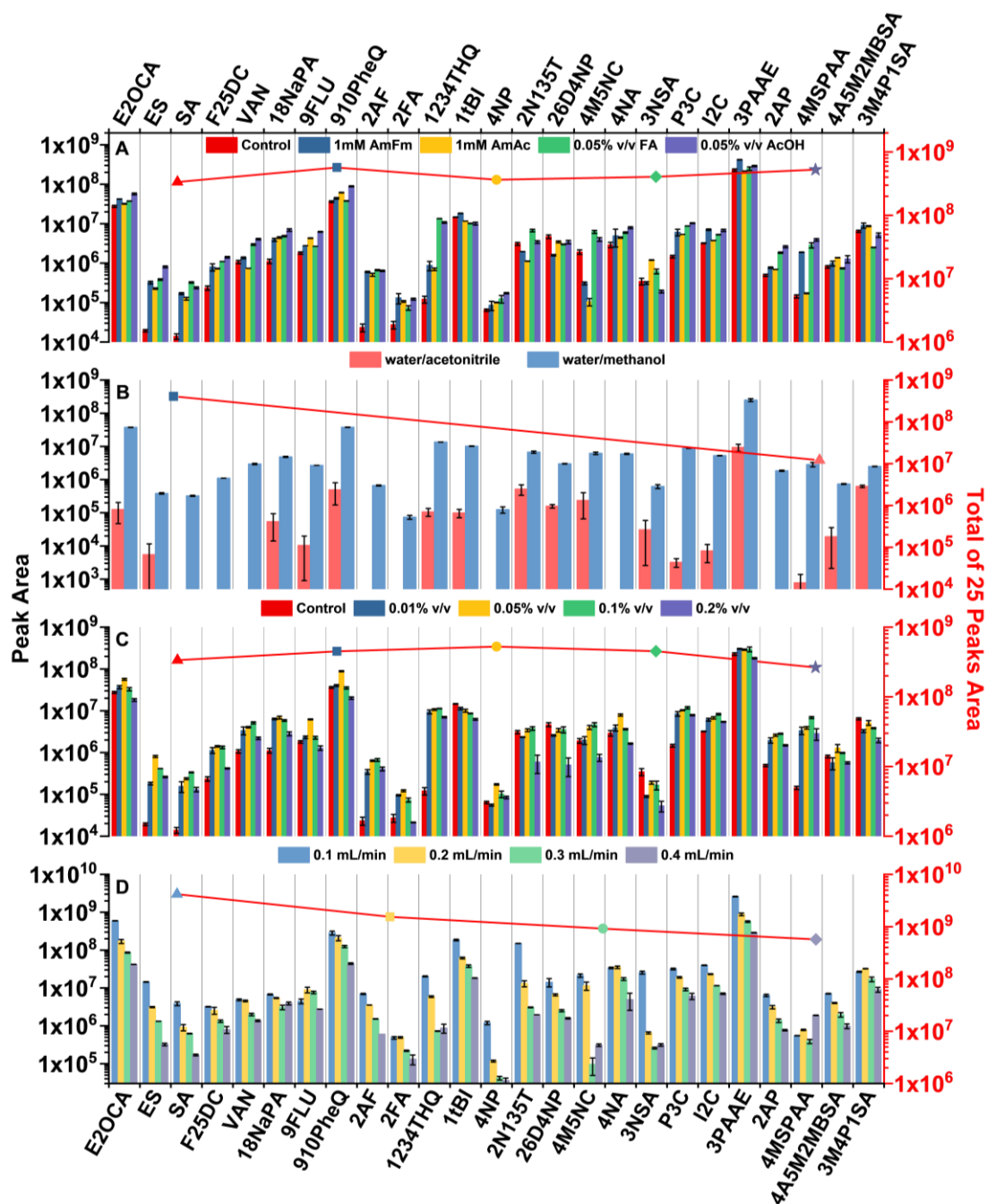


Figure S9. The peak area comparison of 25 reference standards under different type of additives (A), mobile phase (B), additive concentration (C), and flow rate (D).

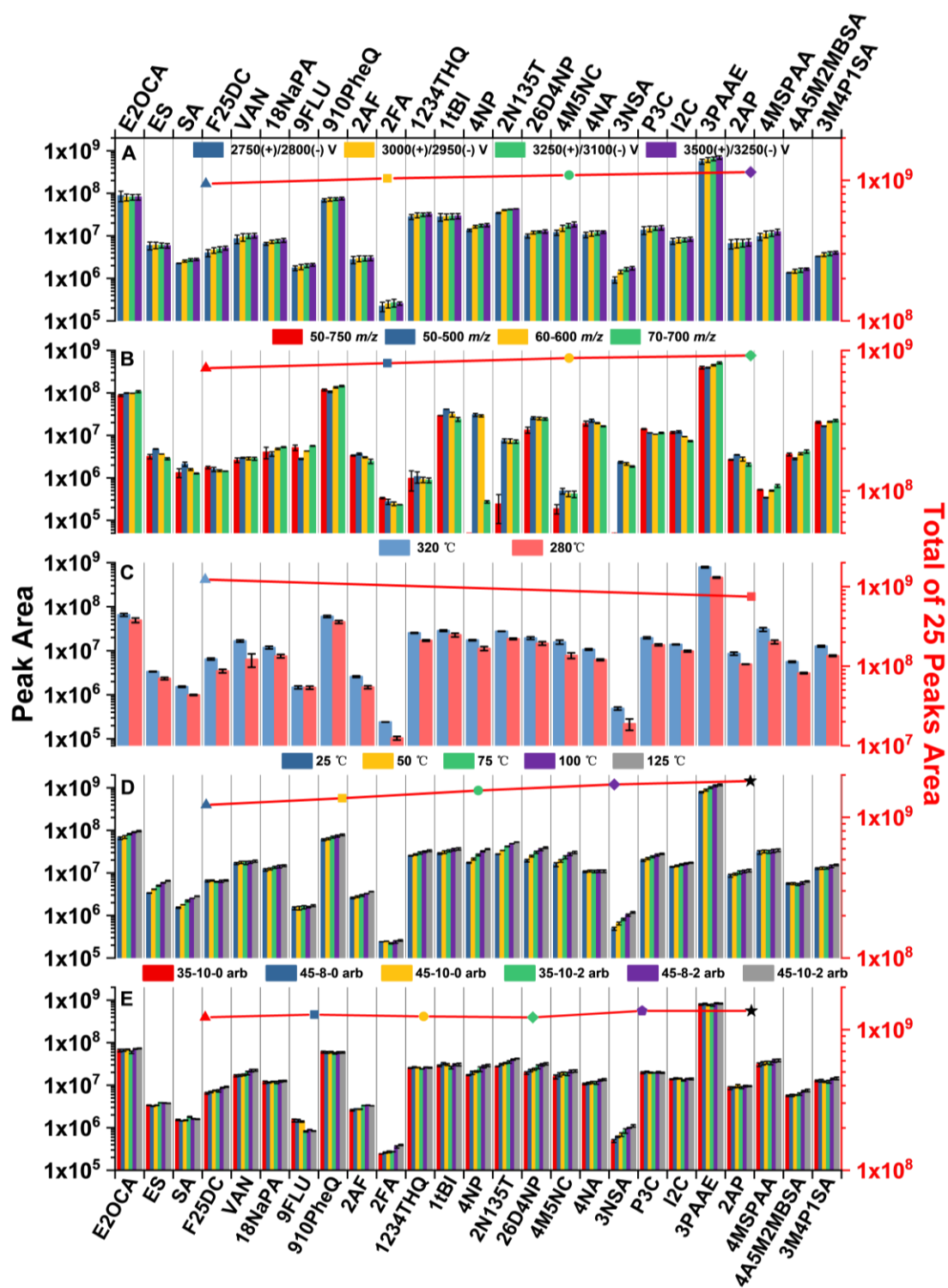


Figure S10. The peak area comparison of 25 reference standards under different voltage (A), mass range (B), temperature of ion transfer tube (C) and vaporizer (D), and the proportion of sheath-auxiliary-sweep gas (E).

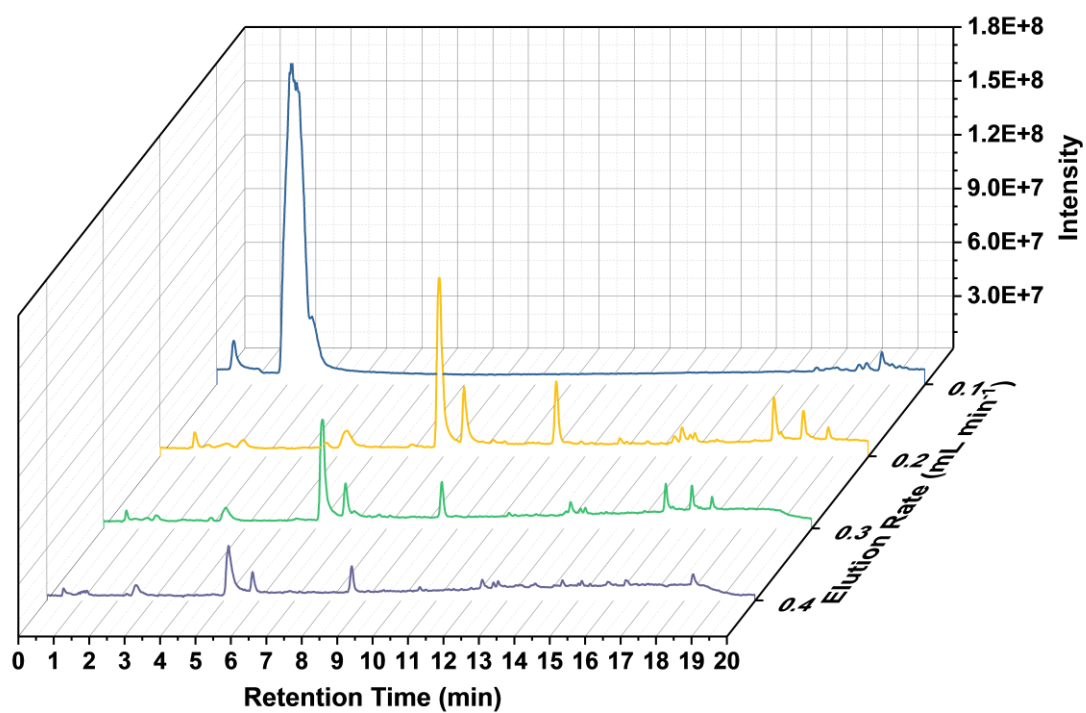


Figure S11. 3D waterfall diagram of total ions chromatogram for mixed standards at different flow rates of mobile phase.

Reference

- Antignac, J. P., De Wasch, K., Monteau, F., De Brabander, H., Andre, F., and Le Bizec, B.: The ion suppression phenomenon in liquid chromatography–mass spectrometry and its consequences in the field of residue analysis, *Anal Chim Acta*, 529, 129–136, <https://doi.org/10.1016/J.ACA.2004.08.055>, 2005.
- Chen, Q., Ikemori, F., Higo, H., Asakawa, D., and Mochida, M.: Chemical Structural Characteristics of HULIS and Other Fractionated Organic Matter in Urban Aerosols: Results from Mass Spectral and FT-IR Analysis, *Environ Sci Technol*, 50, 1721–1730, <https://doi.org/10.1021/ACS.EST.5B05277>, 2016.
- Chow, K. S., Huang, X. H. H., and Yu, J. Z.: Quantification of nitroaromatic compounds in atmospheric fine particulate matter in Hong Kong over 3 years: field measurement evidence for secondary formation derived from biomass burning emissions, *Environmental Chemistry*, 13, 665–673, <https://doi.org/10.1071/EN15174>, 2015.
- Claeys, M., Vermeylen, R., Yasmeen, F., Gómez-González, Y., Chi, X., Maenhaut, W., Mészáros, T., and Salma, I.: Chemical characterisation of humic-like substances from urban, rural and tropical biomass burning environments using liquid chromatography with UV/vis photodiode array detection and electrospray ionisation mass spectrometry, *Environmental Chemistry*, 9, 273–284, <https://doi.org/10.1071/EN11163>, 2012.
- Fan, X., Wei, S., Zhu, M., Song, J., and Peng, P.: Molecular characterization of primary humic-like substances in fine smoke particles by thermochemolysis–gas chromatography–mass spectrometry, *Atmos Environ*, 180, 1–10, <https://doi.org/10.1016/J.ATMOSENV.2018.02.033>, 2018.
- Hettiyadura, A. P. S., Garcia, V., Li, C., West, C. P. C. P., Tomlin, J., He, Q., Rudich, Y., and Laskin, A.: Chemical composition and molecular-specific optical properties of atmospheric brown carbon associated with biomass burning, *Environ Sci Technol*, 55, 2511–2521, <https://doi.org/10.1021/acs.est.0c05883>, 2021.
- Huang, R. J., Yang, L., Shen, J., Yuan, W., Gong, Y., Guo, J., Cao, W., Duan, J., Ni, H., Zhu, C., Dai, W., Li, Y., Chen, Y., Chen, Q., Wu, Y., Zhang, R., Dusek, U., O'Dowd, C., and Hoffmann, T.: Water-Insoluble Organics Dominate Brown Carbon in Wintertime Urban Aerosol of China: Chemical Characteristics and Optical Properties, *Environ Sci Technol*, 54, 7836–7847, <https://doi.org/10.1021/acs.est.0c01149>, 2020.
- Huang, S., Yang, X., Xu, H., Zeng, Y., Li, D., Sun, J., Ho, S. S. H., Zhang, Y., Cao, J., and Shen, Z.: Insights into the nitroaromatic compounds, formation, and light absorption contributing emissions from various geological maturity coals, *Science of The Total Environment*, 870, 162033, <https://doi.org/10.1016/J.SCITOTENV.2023.162033>, 2023.
- Huo, Y., Guo, Z., Li, Q., Wu, D., Ding, X., Liu, A., Huang, D., Qiu, G., Wu, M., Zhao, Z., Sun, H., Song, W., Li, X., Chen, Y., Wu, T., and Chen, J.: Chemical Fingerprinting of HULIS in Particulate Matters Emitted from Residential Coal and Biomass Combustion, *Environ Sci Technol*, 55, 3593–3603, <https://doi.org/10.1021/acs.est.0c08518>, 2021.
- Jaoui, M., Docherty, K. S., Lewandowski, M., and Kleindienst, T. E.: Yields and molecular composition of gas-phase and secondary organic aerosol from the photooxidation of the volatile consumer product benzyl alcohol: Formation of highly oxygenated and hydroxy nitro-Aromatic compounds, *Atmos Chem Phys*, 23, 4637–4661, <https://doi.org/10.5194/ACP-23-4637-2023>, 2023.
- Jemal, M., Ouyang, Z., and Teitz, D. S.: High Performance Liquid Chromatography Mobile Phase Composition Optimization for the Quantitative Determination of a Carboxylic Acid Compound in

Human Plasma by Negative Ion Electrospray High Performance Liquid Chromatography Tandem Mass Spectrometry, [https://doi.org/10.1002/\(SICI\)1097-0231\(19980430\)12:8<429::AID-RCM179>3.0.CO;2-I](https://doi.org/10.1002/(SICI)1097-0231(19980430)12:8<429::AID-RCM179>3.0.CO;2-I), 1998.

Jin Yang, X., Qu, Y., Yuan, Q., Wan, P., Du, Z., Chen, D., and Wong, C.: Effect of ammonium on liquid- and gas-phase protonation and deprotonation in electrospray ionization mass spectrometry, *Analyst*, 138, 659–665, <https://doi.org/10.1039/C2AN36022E>, 2012.

Kamel, A. M., Brown, P. R., and Munson, B.: Effects of mobile-phase additives, solution pH, ionization constant, and analyte concentration on the sensitivities and electrospray ionization mass spectra of nucleoside antiviral agents, *Anal Chem*, 71, 5481–5492, <https://doi.org/10.1021/AC9906429>, 1999.

Kampf, C. J., Jakob, R., and Hoffmann, T.: Identification and characterization of aging products in the glyoxal/ammonium sulfate system – Implications for light-absorbing material in atmospheric aerosols, *Atmos Chem Phys*, 12, 6323–6333, <https://doi.org/10.5194/ACP-12-6323-2012>, 2012.

Kojima, Y., Inazu, K., Hisamatsu, Y., Okochi, H., Baba, T., and Nagoya, T.: Influence of secondary formation on atmospheric occurrences of oxygenated polycyclic aromatic hydrocarbons in airborne particles, *Atmos Environ*, 44, 2873–2880, <https://doi.org/10.1016/J.ATMOSENV.2010.04.048>, 2010.

Kuang, Y., Shang, J., Sheng, M., Shi, X., Zhu, J., and Qiu, X.: Molecular Composition of Beijing PM_{2.5} Brown Carbon Revealed by an Untargeted Approach Based on Gas Chromatography and Time-of-Flight Mass Spectrometry, *Environ Sci Technol*, 57, 909–919, <https://doi.org/10.1021/acs.est.2c05918>, 2023.

Lee, J. Y. and Lane, D. A.: Formation of oxidized products from the reaction of gaseous phenanthrene with the OH radical in a reaction chamber, *Atmos Environ*, 44, 2469–2477, <https://doi.org/10.1016/J.ATMOSENV.2010.03.008>, 2010.

Lesellier, E., Fougere, L., and Poe, D. P.: Kinetic behaviour in supercritical fluid chromatography with modified mobile phase for 5 µm particle size and varied flow rates, *J Chromatogr A*, 1218, 2058–2064, <https://doi.org/10.1016/J.CHROMA.2010.12.057>, 2011.

Li, X., Wang, Y., Hu, M., Tan, T., Li, M., Wu, Z., Chen, S., and Tang, X.: Characterizing chemical composition and light absorption of nitroaromatic compounds in the winter of Beijing, *Atmos Environ*, 237, 117712, <https://doi.org/10.1016/J.ATMOSENV.2020.117712>, 2020a.

Li, X., Hu, M., Wang, Y., Xu, N., Fan, H., Zong, T., Wu, Z., Guo, S., Zhu, W., Chen, S., Dong, H., Zeng, L., Yu, X., and Tang, X.: Links between the optical properties and chemical compositions of brown carbon chromophores in different environments: Contributions and formation of functionalized aromatic compounds, *Science of the Total Environment*, 786, <https://doi.org/10.1016/j.scitotenv.2021.147418>, 2021.

Li, Y., A. Day, D., Stark, H., L. Jimenez, J., and Shiraiwa, M.: Predictions of the glass transition temperature and viscosity of organic aerosols from volatility distributions, *Atmos Chem Phys*, 20, 8103–8122, <https://doi.org/10.5194/ACP-20-8103-2020>, 2020b.

Liang, Y., Guan, T., Zhou, Y., Liu, Y., Xing, L., Zheng, X., Dai, C., Du, P., Rao, T., Zhou, L., Yu, X., Hao, K., Xie, L., and Wang, G.: Effect of mobile phase additives on qualitative and quantitative analysis of ginsenosides by liquid chromatography hybrid quadrupole-time of flight mass spectrometry, *J Chromatogr A*, 1297, 29–36, <https://doi.org/10.1016/J.CHROMA.2013.04.001>, 2013.

Lin, P., Rincon, A. G., Kalberer, M., and Yu, J. Z.: Elemental composition of HULIS in the Pearl River Delta Region, China: Results inferred from positive and negative electrospray high resolution mass spectrometric data, *Environ Sci Technol*, 46, 7454–7462, <https://doi.org/10.1021/es300285d>, 2012.

Louisi, A. P., Nikitas, P., and Zitrou, A.: Modelling flow rate gradient elution in reversed-phase liquid chromatography, *Anal Chim Acta*, 573–574, 305–310, <https://doi.org/10.1016/J.ACA.2006.03.038>, 2006.

Ma, G., Liu, X., Wang, J., Li, M., Dong, Z., Li, X., Wang, L., Han, Y., and Cao, J.: Characteristics and health risk assessment of indoor and outdoor PM_{2.5} in a rural village, in Northeast of China: impact of coal and biomass burning, *Environ Geochem Health*, 45, 9639–9652, <https://doi.org/10.1007/S10653-023-01755-W>, 2023.

Ma, J., Ungeheuer, F., Zheng, F., Du, W., Wang, Y., Cai, J., Zhou, Y., Yan, C., Liu, Y., Kulmala, M., Daellenbach, K. R., and Vogel, A. L.: Nontarget Screening Exhibits a Seasonal Cycle of PM_{2.5} Organic Aerosol Composition in Beijing, *Environ Sci Technol*, 56, 7017–7028, <https://doi.org/10.1021/acs.est.1c06905>, 2022.

Ma, Y., Cheng, Y., Gao, G., Yu, J. Z., and Hu, D.: Speciation of carboxylic components in humic-like substances (HULIS) and source apportionment of HULIS in ambient fine aerosols (PM_{2.5}) collected in Hong Kong, *Environmental Science and Pollution Research*, 27, 23172–23180, <https://doi.org/10.1007/S11356-020-08915-W>, 2020.

Mukherjee, A., Dey, S., Rana, A., Jia, S., Banerjee, S., and Sarkar, S.: Sources and atmospheric processing of brown carbon and HULIS in the Indo-Gangetic Plain: Insights from compositional analysis, *Environmental Pollution*, 267, 115440, <https://doi.org/10.1016/J.ENVPOL.2020.115440>, 2020.

Nasiri, A., Jahani, R., Mokhtari, S., Yazdanpanah, H., Daraei, B., Faizi, M., and Kobarfard, F.: Overview, consequences, and strategies for overcoming matrix effects in LC-MS analysis: A critical review, <https://doi.org/10.1039/d1an01047f>, 2021.

Nguyen, Q. T., Christensen, M. K., Cozzi, F., Zare, A., Hansen, A. M. K., Kristensen, K., Tulinius, T. E., Madsen, H. H., Christensen, J. H., Brandt, J., Massling, A., Nøjgaard, J. K., and Glasius, M.: Understanding the anthropogenic influence on formation of biogenic secondary organic aerosols in Denmark via analysis of organosulfates and related oxidation products, *Atmos Chem Phys*, 14, 8961–8981, <https://doi.org/10.5194/ACP-14-8961-2014>, 2014.

Nozière, B., Kalberer, M., Claeys, M., Allan, J., D’Anna, B., Decesari, S., Finessi, E., Glasius, M., Grgić, I., Hamilton, J. F., Hoffmann, T., Iinuma, Y., Jaoui, M., Kahnt, A., Kampf, C. J., Kourtchev, I., Maenhaut, W., Marsden, N., Saarikoski, S., Schnelle-Kreis, J., Surratt, J. D., Szidat, S., Szmigielski, R., and Wisthaler, A.: The Molecular Identification of Organic Compounds in the Atmosphere: State of the Art and Challenges, *Chem Rev*, 115, 3919–3983, <https://doi.org/10.1021/CR5003485>, 2015.

Nyiri, Z., Novák, M., Bodai, Z., Szabó, B. S., Eke, Z., Zárny, G., and Szigeti, T.: Determination of particulate phase polycyclic aromatic hydrocarbons and their nitrated and oxygenated derivatives using gas chromatography–mass spectrometry and liquid chromatography–tandem mass spectrometry, *J Chromatogr A*, 1472, 88–98, <https://doi.org/10.1016/J.CHROMA.2016.10.021>, 2016.

Pan, X., Tian, K., Jones, L. E., and Cobb, G. P.: Method optimization for quantitative analysis of octahydro-1,3,5,7-tetranitro-1,3,5,7-tetrazocine (HMX) by liquid chromatography-electrospray

ionization mass spectrometry, *Talanta*, 70, 455–459,
<https://doi.org/10.1016/J.TALANTA.2006.03.005>, 2006.

Petters, M. D. and Kreidenweis, S. M.: A single parameter representation of hygroscopic growth and cloud condensation nucleus activity, *Atmos Chem Phys*, 7, 1961–1971,
<https://doi.org/10.5194/ACP-7-1961-2007>, 2007.

Pizzutti, I. R., Vela, G. M. E., De Kok, A., Scholten, J. M., Dias, J. V., Cardoso, C. D., Concenço, G., and Vivian, R.: Determination of paraquat and diquat: LC-MS method optimization and validation, *Food Chem*, 209, 248–255, <https://doi.org/10.1016/j.foodchem.2016.04.069>, 2016.

Song, W. Y., Park, H., and Kim, T. Y.: Improving liquid chromatography-mass spectrometry sensitivity for characterization of lignin oligomers and phenolic compounds using acetic acid as a mobile phase additive, *J Chromatogr A*, 1685, 463598,
<https://doi.org/10.1016/J.CHROMA.2022.463598>, 2022.

Stone, E. A., Hedman, C. J., Sheesley, R. J., Shafer, M. M., and Schauer, J. J.: Investigating the chemical nature of humic-like substances (HULIS) in North American atmospheric aerosols by liquid chromatography tandem mass spectrometry, *Atmos Environ*, 43, 4205–4213,
<https://doi.org/10.1016/J.ATMOSENV.2009.05.030>, 2009.

Tao, H., Tang, T., Wang, H., Huo, T., Yang, H., and Zhou, Y.: Characterization of atmospheric nitroaromatic compounds in Southwest China by direct injection liquid chromatography-tandem mass spectrometry analysis of aerosol extracts, *Chemosphere*, 363, 142845,
<https://doi.org/10.1016/J.CHEMOSPHERE.2024.142845>, 2024.

Voliotis, A., Prokeš, R., Lammel, G., and Samara, C.: New insights on humic-like substances associated with wintertime urban aerosols from central and southern Europe: Size-resolved chemical characterization and optical properties, *Atmos Environ*, 166, 286–299,
<https://doi.org/10.1016/J.ATMOSENV.2017.07.024>, 2017.

Wang, X., Gu, R., Wang, L., Xu, W., Zhang, Y., Chen, B., Li, W., Xue, L., Chen, J., and Wang, W.: Emissions of fine particulate nitrated phenols from the burning of five common types of biomass, *Environmental Pollution*, 230, 405–412, <https://doi.org/10.1016/J.ENVPOL.2017.06.072>, 2017a.

Wang, Y., Hu, M., Lin, P., Guo, Q., Wu, Z., Li, M., Zeng, L., Song, Y., Zeng, L., Wu, Y., Guo, S., Huang, X., and He, L.: Molecular Characterization of Nitrogen-Containing Organic Compounds in Humic-like Substances Emitted from Straw Residue Burning, *Environ Sci Technol*, 51, 5951–5961,
<https://doi.org/10.1021/acs.est.7b00248>, 2017b.

Wang, Y., Hu, M., Lin, P., Tan, T., Li, M., Xu, N., Zheng, J., Du, Z., Qin, Y., Wu, Y., Lu, S., Song, Y., Wu, Z., Guo, S., Zeng, L., Huang, X., and He, L.: Enhancement in Particulate Organic Nitrogen and Light Absorption of Humic-Like Substances over Tibetan Plateau Due to Long-Range Transported Biomass Burning Emissions, *Environ Sci Technol*, 53, 14222–14232,
<https://doi.org/10.1021/acs.est.9b06152>, 2019.

Yan, J., Wang, X., Gao, S., Gong, P., Dotel, J., and Pokhrel, B.: Diagnostic ratio of nitrated phenols as a new method for the identification of pollution emission sources, *Environmental Pollution*, 316, 120509, <https://doi.org/10.1016/J.ENVPOL.2022.120509>, 2023.

Zhang, T., Shen, Z., Huang, S., Lei, Y., Zeng, Y., Sun, J., Zhang, Q., Ho, S. S. H., Xu, H., and Cao, J.: Optical properties, molecular characterizations, and oxidative potentials of different polarity levels of water-soluble organic matters in winter PM_{2.5} in six China’s megacities, *Science of The Total Environment*, 853, 158600, <https://doi.org/10.1016/J.SCITOTENV.2022.158600>, 2022.

Zhou, Y., West, C. P., Hettiyadura, A. P. S., Pu, W., Shi, T., Niu, X., Wen, H., Cui, J., Wang, X., and

417 Laskin, A.: Molecular Characterization of Water-Soluble Brown Carbon Chromophores in
418 Snowpack from Northern Xinjiang, China, *Environ Sci Technol*, 56, 4173–4186,
419 <https://doi.org/10.1021/acs.est.1c07972>, 2022.